Buckling Hydrogenated Biphenylene Network with Tremendous Stretch Extent and Anomalous Thermal Transport Properties

Xiaowei Zhang, Markos Poulos, Konstantinos Termentzidis, Yang Han, Donglei Zhao, Tengfei Zhang, Xiaochuang Liu, Shijie Jia, Guolei Zhang

Buckling Hydrogenated Biphenylene Network with Tremendous Stretch Extent and Anomalous Thermal Transport Properties

Xiaowei Zhang[1], Markos Poulos[2], Konstantinos Termentzidis[2], Yang Han[1,3*], Donglei Zhao[1], Tengfei Zhang[1], Xiaochuang Liu[1], Shijie Jia[1,3], Guolei Zhang[3]

[1]*Qingdao Innovation and Development Center of Harbin Engineering University, 266400 Qingdao, China*

[2]*Université Claude Bernard Lyon, CNRS, INSA-Lyon, CETHIL UMR5008, F-69621, Villeurbanne, France*

[3]*College of Power and Energy Engineering, Harbin Engineering University, 150001 Harbin, China*

Abstract

Hydrogen adsorption is a popular and flexible method to regulate the physical properties of two-dimensional (2D) material like recently synthesized biphenylene networks. In this study, mechanical properties and the thermal conductivity (κ) of the fully hydrogenated biphenylene network (HBPN) under strain were investigated systematically by molecular dynamics (MD) simulation and Wave-packet (WP) Propagation method. It was found that HBPN could sustain an unusual strain as large as 28.8% and 34.5% along the zigzag and armchair directions, respectively, which were much larger than the other 2D buckling structure like silicene (about 19.5% and 17%, respectively). Besides, the κ of HBPN exhibited an anomalous response to uniaxial tensile strain. Different from its mother structure like graphene, the κ of HBPN had an increasing trend with strain explained here with the phononic density of states (PDOS). The physical mechanism behind this non-trivial thermomechanical behavior

*Corresponding Author. E-mail: yhan@hrbeu.edu.cn

of this planar sp^2 hybridized carbon allotrope was related to the following two factors. Firstly, the increase of the number of phonons excited at low frequency region which in general carried more energy and secondly the reduction of the number of higher-frequency phonons thus the weakening of the phonon-surface scattering both helped increase the thermal conductivity under strain. Moreover, the strain induced flattening of the structure was another reason to weaken the coupling between phonons with in-plane and curvature vibrational modes. WP Propagation method within MD was also employed to analyze the propagation of phonons inside the HBPN and group velocities, phonon lifetimes and mean free paths were obtained. Our research can provide essential reference for the application of 2D materials in the field of electronic cooling devices and the modification of thermoelectric energy conversion efficiency of materials.

Keywords: mechanical property, thermal transport property, hydrogenated biphenylene network, tensile strain, equilibrium molecular dynamics simulation, wave-packet propagation

I. Introduction

Since the advent of graphene, two-dimensional (2D) nanomaterials have been widely applied in much smaller, denser, more flexible and efficient nanoelectronic devices and energy materials industries based on their superior characteristics[1–3]. At present, numerous theoretical predictions and experimental investigations have been conducted on the newly synthesized 2D biphenylene network, a non-benzene carbon allotrope which is composed of all sp^2-hybrid carbon atoms with periodic arrangement of 4, 6 and 8 membered rings[4]. For example, many researchers performed experiments to grow a biphenylene network (BPN) through surface copolymer dehydrofluorination (HF-zipper) reaction[5–8]. Wang *et al*.[9] studied the properties of optical and acoustic phonons in monolayer BPN, demonstrating the promising potential of monolayer BPN in applications such as phonon lasers, quantum nonlinear elements and quantum mechanical resonators. Besides, this novel 2D carbon allotrope is of potential application value in lithium storage and carbon-based circuits and it becomes gradually a candidate material for fuel cells according to previous study[10].

Nowadays, new materials with desired thermal transport properties forecast are strongly expected and required. The progress of science and technology drives to continuous electronic devices miniaturization and integration[11], which results to excessively dense electronic devices thus generation of uncurbed heat. Extremely high temperature will affect the stability, reliability and finally the lifetime of electronic devices[12]. Therefore, nano-scale thermal management has become a key factor in the design of modern nano-electronic devices. The high thermal conductivity (κ) of carbon-based 2D materials could help to solve the heat dissipation problem of nanodevices. By equilibrium molecular

dynamics (EMD) method, Ying *et al.*[8] calculated the κ of BPN in zigzag and armchair directions using the Tersoff potential function, getting the results of 226.3 and 232.3 $Wm^{-1}K^{-1}$, respectively.

It is intriguing that the exceptional properties of 2D materials can be regulated by strategies such as structural transformation, stacking fault, defects, adsorption, external strain and electric fields. For example，Mo *et al.*[13] designed the band shape of BPN by fluorinating it by adsorbing fluorine atoms to regulate its electronic properties in BPN applications. Son *et al.*[14] showed that BPN has interesting low energy states such as the zone-center van Hove singularity and near-critical tilted Dirac cones and these two states undergo topological transitions by merging themselves under strains. Hou *et al.*[15] investigated the effect of strain on the electronic properties and phonon frequency of BPN, demonstrating that lattice strain can alter the contact resistance between BPN and electrodes. Ren *et al.*[16] investigated the effects of BN doping on the mechanical properties and anisotropy of BPN. Among them, B doping changed the in-plane distribution of BPN mechanical properties, while N doping significantly enhanced the anisotropy of BPN mechanical properties. Based on the first-principles, Xie *et al.*[17] studied the effect of hydrogen adsorption on the stability of BPN, indicating that fully hydrogenation is the most structurally stable hydrogenation method when analyzing the thermal transport properties which sparked our great interest. Meanwhile, experiments have shown that it is feasible to attach atoms to two-dimensional lattices or surfaces at the microscopic level. González-Herrero *et al.*[18] and Slot *et al.*[19] demonstrated that using scanning tunneling microscopy (STM), hydrogen atoms or carbon monoxide molecules could be absorbed and controlled at the atomic scale on graphene or copper surfaces, while some others showed that their adsorption positions could

even be freely manipulated[20]. Therefore, the synthesis of HBPN could be possibly achieved in experiments.

In practical applications, materials will be applied under different working conditions. Different harsh temperature and pressure conditions usually cause various effects on the properties of materials. Unsuitable working conditions leads to strain of the material (bending, torsion or even fracture). The tensile strain under different conditions will also affect thermal transport properties of materials. Therefore, it is particularly essential to study heat transfer of HBPN under strain. Actually, axial tension is more suitable for studying the tensile properties, fracture behavior and stress-strain relationship of materials, while plane shear is more suitable for studying the slip, deformation mechanisms and rheological properties of materials. The purpose of this work aims to investigate the tensile performance of HBPN so we chose the axial tension to apply. Compared with biaxial tensile strain, the uniaxial one is more practical, flexible and much easier to achieve in experiments. Based on the planer 2D structure of BPN and its symmetry, only the uniaxial tension effect was considered here in our work.

The rest of this paper is organized as follows. Firstly, simulation model and computational method are described in Sec. 2. Then in Sec. 3, results and discussions on structure stability, mechanical properties, thermal and phonon wave-packet transport properties are systematically given. Finally, in Sec. 4, the paper finishes with a summary and conclusions.

II. Simulation model and computational method

A. Geometric structure model

The structure of pristine BPN is shown in Fig. 1(a). The unit cell is composed of six carbon atoms. The initial lattice constants are a = 3.750 Å and b = 4.520 Å with characteristic C-C bond lengths of $d1$ = 1.450 Å, $d2$ = 1.450 Å, $d3$ = 1.410 Å and $d4$ = 1.460 Å which are consistent with previous result [21]. Zigzag/armchair are along the *x/y* directions respectively and it also represents the direction in which strain is loaded. The unit cell model used for hydrogenation is a 2 × 2 × 1 supercell which contains 24 sp^2-hybridized C atoms in total. We used the adaptive empirical bond order (AIREBO[22]) potential to simulate the interaction between C-C and C-H atoms. This potential is of the three-body type and suitable for simulating breaking and creating of bonds in hydrocarbon system[23]. In agreement with previous studies, the preferential energetically hydrogen adsorption positions are alternated on the *xy* plane for neighboring carbon atoms[17]. Here we consider as many as 12 adsorption structures and obtained its corresponding energies *c.f.* the detailed information in the supplementary material SI. We eventually verified that the fully hydrogenation mode is the most stable one as shown in Fig.1(b), further proving that the MD result is consistent with that of first principles[17,24]. So we employed a fully hydrogenated configuration as our computational model. A vacuum region of 20 Å was added to the original thickness d in z direction of the box to avoid interlayer atomic interactions caused by periodic boundary conditions. After energy minimization, the lattice constants of the fully hydrogenated configuration model became $2a$ = 2 × 3.905 Å = 7.810 Å and $2b$ = 2 × 4.5585 Å = 9.117 Å. To check the structure parameters of MD results, we also optimized the structure by density function theory (DFT) calculations obtaining lattice parameter of a = 3.865 Å and b = 4.624 Å, respectively. Compared with DFT result, the lattice values from MD are slightly deviated from those of DFT (+1.03% and -

1.42% for *a* and *b*, respectively). However, the final optimized configuration structures obtained from the two methods are similar, meaning that the empirical potential of MD employed in our simulations could reproduce the ideal structure of the fully hydrogenated configuration. Besides, it is worth noting that the real thickness of the model after hydrogen adsorption to the BPN should be defined to acquire the real V of the model. We took the distance between the top and bottom H layers (parameter "*d*" donated in Fig. 1(b)) plus the van der Waals diameter of H atom[25,26] as the real thickness. The initial layer thickness of HBPN is 5.14 Å. We used a 10 × 8 × 1 large supercell with a total of 3840 (6 × 2 × 2 × 1 × 2 × 10 × 8 × 1) atoms as the initial simulation model in our work.

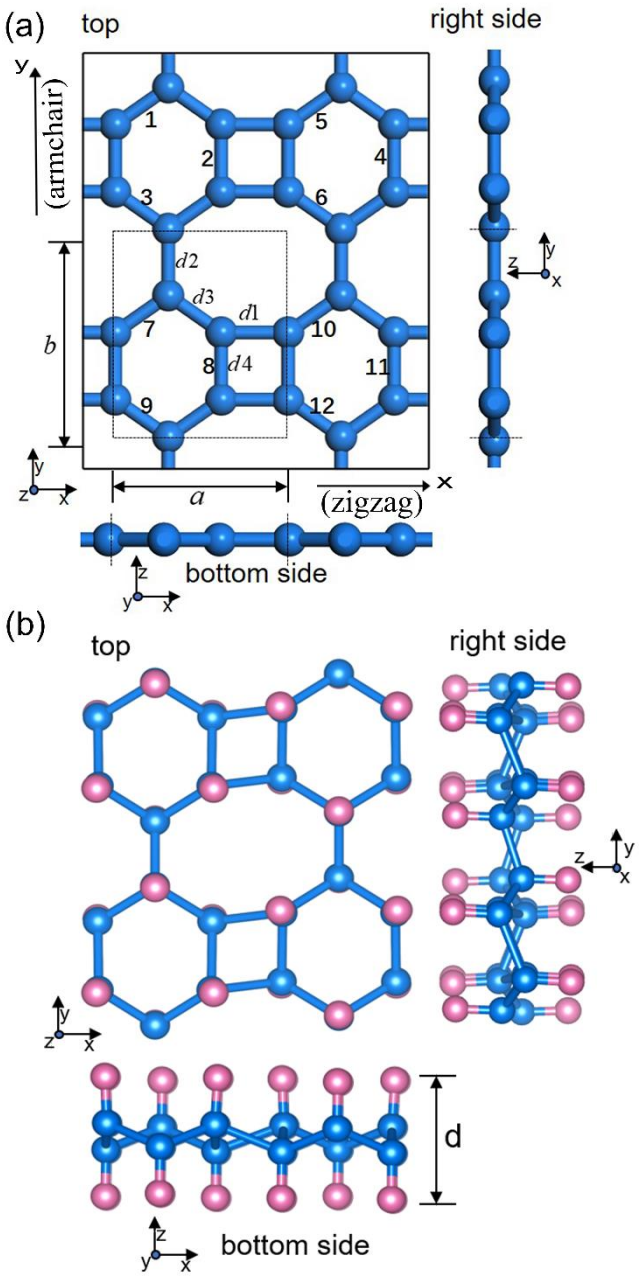

Figure 1. Perspective views of (a) biphenylene network (BPN) and (b) fully hydrogenated biphenylene network structures with C and H atom represented by blue and pink ball, respectively. The black solid rectangular boxes are the unit cells. *d*1 - *d*4 are the bond lengths in the original pristine configuration BPN. *d* is the distance between the two most upper and lower hydrogen atoms of the fully hydrogenated configuration. Numbers 1 - 12 denote 12 adsorption positions, *c.f.* supplementary information SI for more details.

B. Phonon dispersion from DFT calculations

To optimize the hydrogenated structure by DFT method and compare the lattice parameters obtained with those from MD, we performed First-principles calculations by VASP[27]. PBE exchange-correlation energy in GGA[28,29] with projected augmented wave (PAW) method was utilized[29,30]. A kinetic energy cutoff value as large as 600 eV was employed for the plane-wave basis set. A dense enough Monkhorst-Pack[31] *k*-points (21×35×1) in the 1st Brillouin zone was sampled to get an accurate converged energy value via the conjugate-gradient algorithm[32]. For the electron self-consistent loop, the tolerance of total energy was set to be 10^{-8} eV. Finally, the force on each atom converged to be less than 10^{-5} eV/Å after optimization. To check the structure's mechanical stability, phonon dispersion curve was obtained via Phonopy code[33] by inputting the harmonic interaction force constants.

C. Thermal conductivity calculation from Green-Kubo method

About mechanical properties calculations, uniaxial stretching was loaded in each direction of the structure in order to obtain stress *vs.* strain curves. Then fluctuation dissipation theorem combined with Green-Kubo method (EMD)[34,35] was used to calculate the κ of the stable configurations of HBPN under different strains. This method calculated the running thermal conductivity $\kappa(t)$ by integrating the heat current autocorrelation function (HCACF) over a given correlation time t.

$$\kappa(t) = \frac{1}{k_B T^2 V} \int_0^t \langle J(0) J(\tau) \rangle d\tau \tag{1.1}$$

Where k_B is Boltzmann's constant and $\langle J(0) J(\tau) \rangle$ is the average HCACF over different time origins with J being the heat current. We considered domain sizes up to 10 × 8 × 1 cubic conventional cells for HBPN. Periodic boundary conditions were applied in *x*, *y*, and *z* directions. The Verlet algorithm

was used to integrate the equations of motion with 0.25 fs time step which was checked to be small enough. In all simulations, the atomic systems were first equilibrated in a NVT ensemble for 50 ps before being switched to a NVE ensemble for another 2.5 ns. Berendsen barostat and thermostat[36,37] were used to control the pressure and the temperature of the system during equilibration runs. Then, the following 2.5 ns simulation in NVE ensemble was taken for data production. The flux fluctuations were computed each 2.5 fs and the integral was sampled over 20000 values. The correlation time upper limit of our calculations was chosen to be 500 ps. Each simulation ran for 10 times with independent initial velocity distributions. It was an inherent assumption in this study that 10 independent simulations provided a representative sample for the relevant statistical analysis. Finally, we report the average of the 10 independent MD runs as the predicted thermal conductivity and the standard error as its uncertainty.

D. Phononic density of states analysis

PDOS (phononic density of states, also known as vibrational density of states (VDOS)) under uniaxial strain was calculated to further analyze the behavior of thermal transport properties of the strained HBPN. The change of wave crest in the density distribution diagram of phonon states directly reflected the change of the number and modes of phonons (the change of peak value reflected the change of the number of phonons and the movement of wave crest reflected the change of phonon mode), thus characterizing the vibration strength of atoms. PDOS were calculated by Fourier transform of the atomic velocity autocorrelation function, which was defined as follows[38]:

$$PDOS(\omega) = \frac{1}{\sqrt{2\pi}} \int_0^\infty e^{i\omega t} C(t)\, dt \qquad (1.2)$$

where ω and C(t) represent angular frequency and the velocity auto-correlation function, respectively.

In the calculations of the total PDOS, C(t) was obtained by:

$$C(t)=\left\langle \sum_{j=1}^{N} \vec{v_j}(0)\cdot\vec{v_j}(t) \right\rangle \tag{1.3}$$

Where $v_j(t)$ represents the velocity of atom j, and ⟨ ⟩ is used to describe the ensemble average.

E. Wave-packet propagation simulations

To study the propagation of phonons inside the pristine material, we have employed the Wave-packet Propagation method (WP) within Molecular Dynamics, in which a mechanical excitation was imposed on the atoms of a small region and the propagation of the injected energy was monitored with time. This method has been already applied to study heat transport in a variety of systems such as amorphous silicon-like materials[39], silicon nanocomposites[40], asymmetric two-phase silicon nanowires[41], core-shell silicon nanowires[42] and others. In this work we aimed to study the propagation of phonons in HBPN from all three acoustic branches (LA, TA, ZA), along both principal directions (armchair and zigzag), for three different strain states: unstrained, strained along zigzag (ε=20%) and strained along armchair (ε=25%). All calculations were performed under a temperature of T=300 K. As excitation, we have chosen a Gaussian-modulated sinusoidal force:

$$\vec{F_i} = A\vec{e_i}\sin\left[2\pi\nu\left(t-3\tau\right)\right]\cdot\exp\left[\frac{\left(t-3\tau\right)^2}{\left(2\tau\right)^2}\right] \tag{1.4}$$

The pulse is characterized by its frequency f, amplitude A, polarization vector $\vec{e}$ and width τ, which is the standard deviation of the Gaussian envelope. The pulse is displaced by three widths τ towards negative times, so that at $t=0$ the force is practically zero. By modifying f we can select the phonon mode that we want to excite. In our case, we have chosen $f=2THz$ for all simulations, in

order to excite all the three acoustic branches. Furthermore, by choosing the polarization vector to be in-plane and parallel or perpendicular to the propagation direction, we can selectively excite the LA or TA phonons respectively, and by choosing it to be perpendicular to the sheet plane, we excite the flexural ZA phonons. In its turn, the propagation direction coincides with the normal to the plane of the excitation region. The width τ of the Gaussian window controls the time duration of the pulse and by extent, its spatial extension. On the other hand, as is well known, the temporal extension is inversely proportional to the frequency resolution, so in the end τ must be chosen while maintaining an equilibrium between spatiotemporal localization and a good frequency resolution. In this work all pulses had a width of τ=$0.15\,ps$, which corresponds to a frequency resolution $\Delta\nu \approx 1/2\pi\tau \approx 1THz$. Finally, the choice of the amplitude A can impact the calculation in two different ways: a very small amplitude results in a weak pulse that does not contrast well with the thermal background (for systems at non-zero temperature), while a very large amplitude induces nonlinear anharmonic effects that change the effective properties of the system in an unpredictable manner. In all the simulated configurations it has been noticed that with the same force amplitude, the excited in-plane modes have a much smaller displacement amplitude than the flexural ones. So in order to avoid non-linear effects for the ZA packets and keep a good contrast for the in-plane packets, we have applied A=$0.5eV/\AA$ for the flexural and A=$0.3eV/\AA$ for the in-plane packets.

The systems studied were HBPN ribbons at 300 K, approximately 75 nm long and under three different strain states: unstrained, 20% strain along the armchair axis, and 25% strain along the zigzag axis. In each of those strain states, acoustic phonon wave packets were launched with wave vectors along both the armchair and the zigzag symmetry axes and for both of them, all three polarisations

(LA, TA, ZA) were tested. In total, combining the simulations for wave vectors along both symmetry axes, having all three polarizations and for the three strain states mentioned above, we performed 18 runs. In all of them, Periodic Boundary Conditions were applied along the in-plane directions. AIREBO was employed as interatomic potential, and the timestep was chosen to be 0.5 fs. The system was left to evolve for 10000 timesteps, totaling 5 ps of simulation time.

III. Results & Discussion

A. Mechanical properties

Before studying any physical properties of materials, stability of the structure should be checked in advance[43,44]. Firstly, to check the mechanical stability of the fully HBPN, phonon dispersions of the structure were calculated from DFT calculations as given in Fig. 2. There were no imaginary frequencies in the phonon dispersion curves proving that the structure is thermo-dynamic stable.

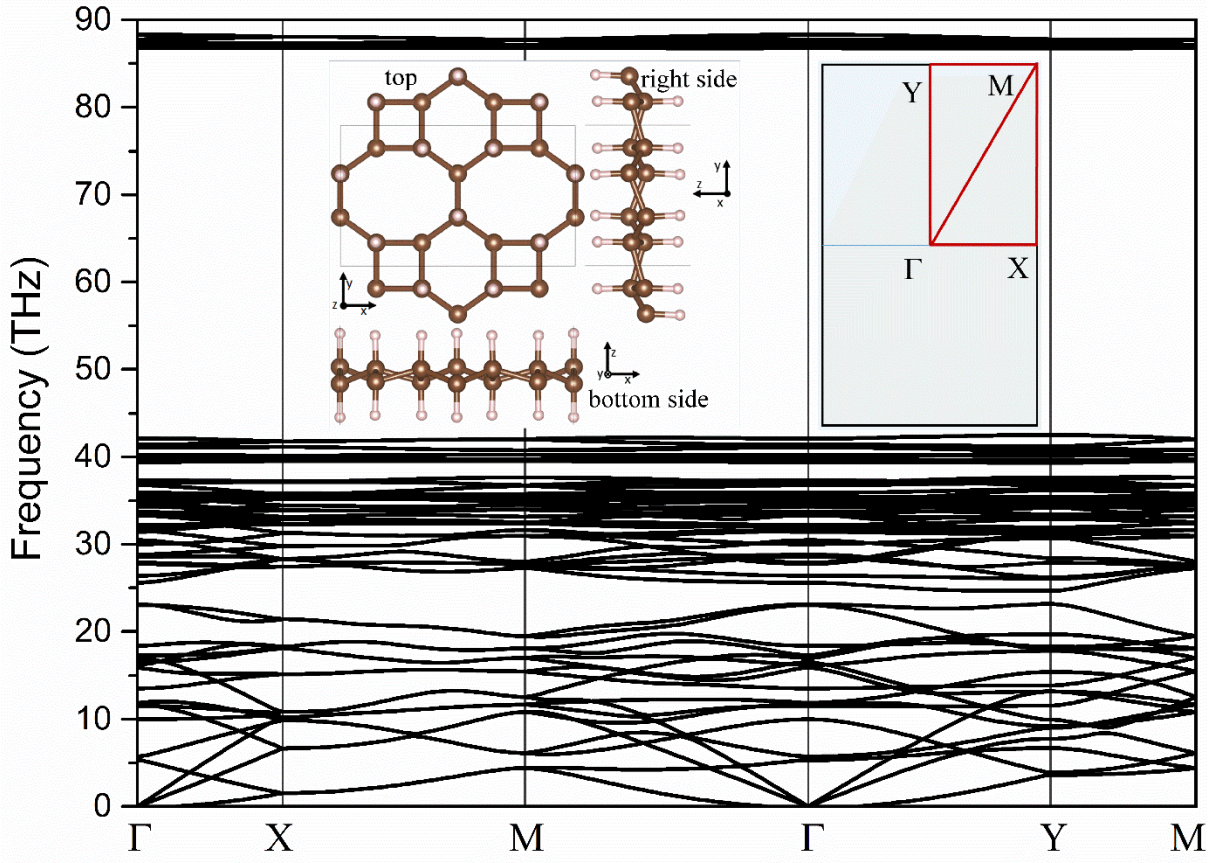

Figure 2. Phonon dispersion curves of fully HBPN. The top and side views of the structure present as insets. The first Brillouin zone with high symmetry points and routines noted also appears.

Recently, Mashhadzadeh[7] and Samadian *et al.*[45] have both used the MD method to calculate some mechanical properties of BPN, indicating that MD is sufficiently reliable in calculating the mechanical properties of BPN materials. To study the mechanical properties of HBPN, the structure was stretched in uniaxial zigzag and armchair directions, respectively. A total of three independent stretches were carried out, and the results were generally consistent with each other. The obtained stress values versus strain curves from a set of data are shown in Fig. 3. From the latter figure, we can see that breaks occurred when the strain rates reached 28.8% and 34.5% along the zigzag and armchair directions, respectively. So thermal transport properties of the structure under strain were studied within the fracture ranges. Besides, Young's modulus values for different directions were obtained by linear fitting

of stress *vs.* strain curves within the range of $\varepsilon < 5\%$. Along zigzag and armchair directions, Young's modulus values were calculated to be 325.47 ± 1.868 and 264.174 ± 2.570 GPa, respectively, which were much smaller than those values of pristine BPN from previous result (650 and 574 GPa[7], respectively). Note that the value along the zigzag direction was bigger than that along the armchair one. From the structure point of view, angle rotational freedom range is smaller in the zigzag direction than in the armchair one, that's why the structure suffered bigger stress and fractured earlier when strain was loaded in the zigzag direction than in the armchair one.

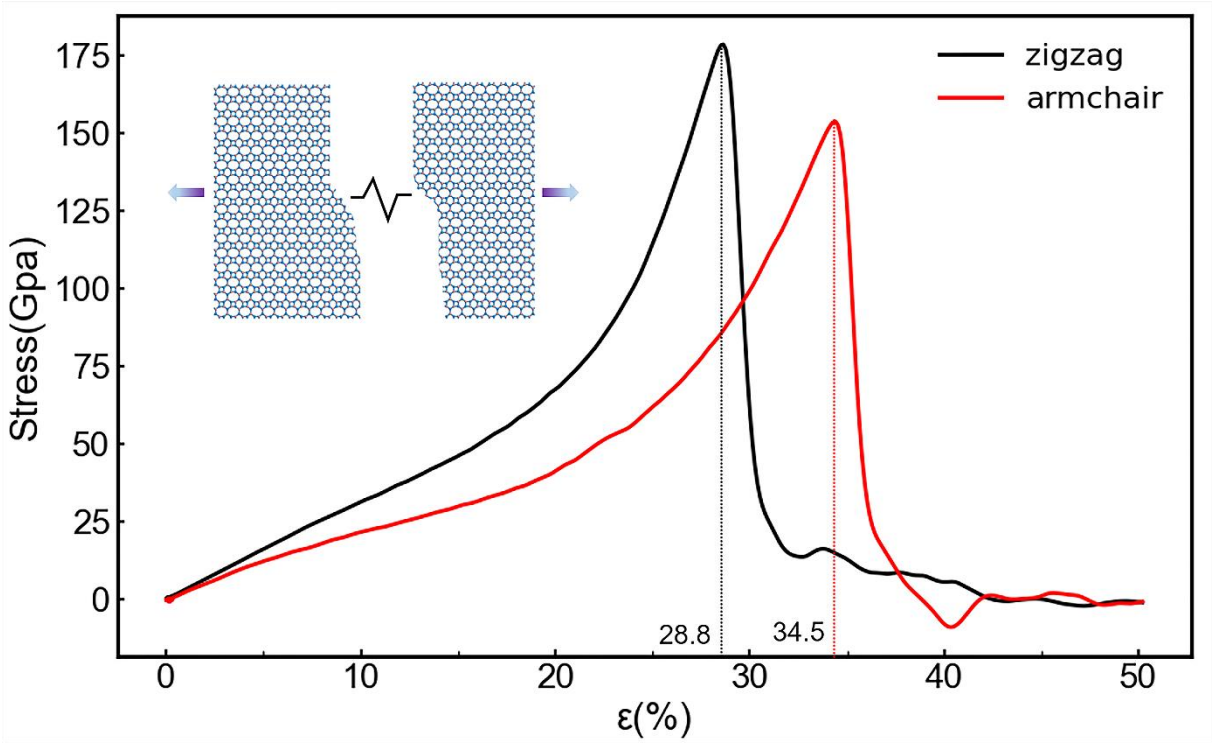

Figure 3. Stress of HBPN under different strains along the zigzag (black solid line) and armchair (red solid line) directions, respectively. The dotted lines at $\varepsilon \approx 28.8$ % and 34.5 % correspond to the tensile fracture points of the model which are the maximum stress-strain points. The illustration represents the schematic diagram of HBPN under uniaxial stretching in the zigzag direction.

B. Thermal transport properties of HBPN under mechanical tension

The thermal conductivity in nanostructures is an extrinsic property, thus size dependent [46,47]. The result from EMD method to get thermal conductivity is less dependent on the size of the structure than the NEMD one. A 10 × 8 × 1 large enough supercell with a total of 3840 atoms was used, after we have checked the convergence. The obtained $\kappa \pm \Delta\kappa$ ($\kappa_x \pm \Delta\kappa_x$ = 17.258 ± 2.898 $Wm^{-1}K^{-1}$ and $\kappa_y \pm \Delta\kappa_y$ = 19.208 ± 1.822 $Wm^{-1}K^{-1}$) is the result of 10 statistically independent runs with the corresponding standard error $\Delta\kappa$ to achieve a good statistical accuracy. The κ in the armchair direction is slightly larger than that in the zigzag direction when it is not stretched, which is the same as the κ of BPN obtained from previous studies[8]. Fig. 4 gives the normalized heat current autocorrelation function (HCACF) for one example run and all running integrals and their average over 10 statistically independent runs for the unstrained HBPN. The HCACF degrades quickly to zero with a small uncertainty on the final estimate of the thermal conductivity value upon averaging. For the sake of clarity, the zooming-in view of the HCACF at the beginning of integral was also laid on the panel. The standard errors of the thermal conductivity values of HBPN under all strains in each direction were found to be less than 10%.

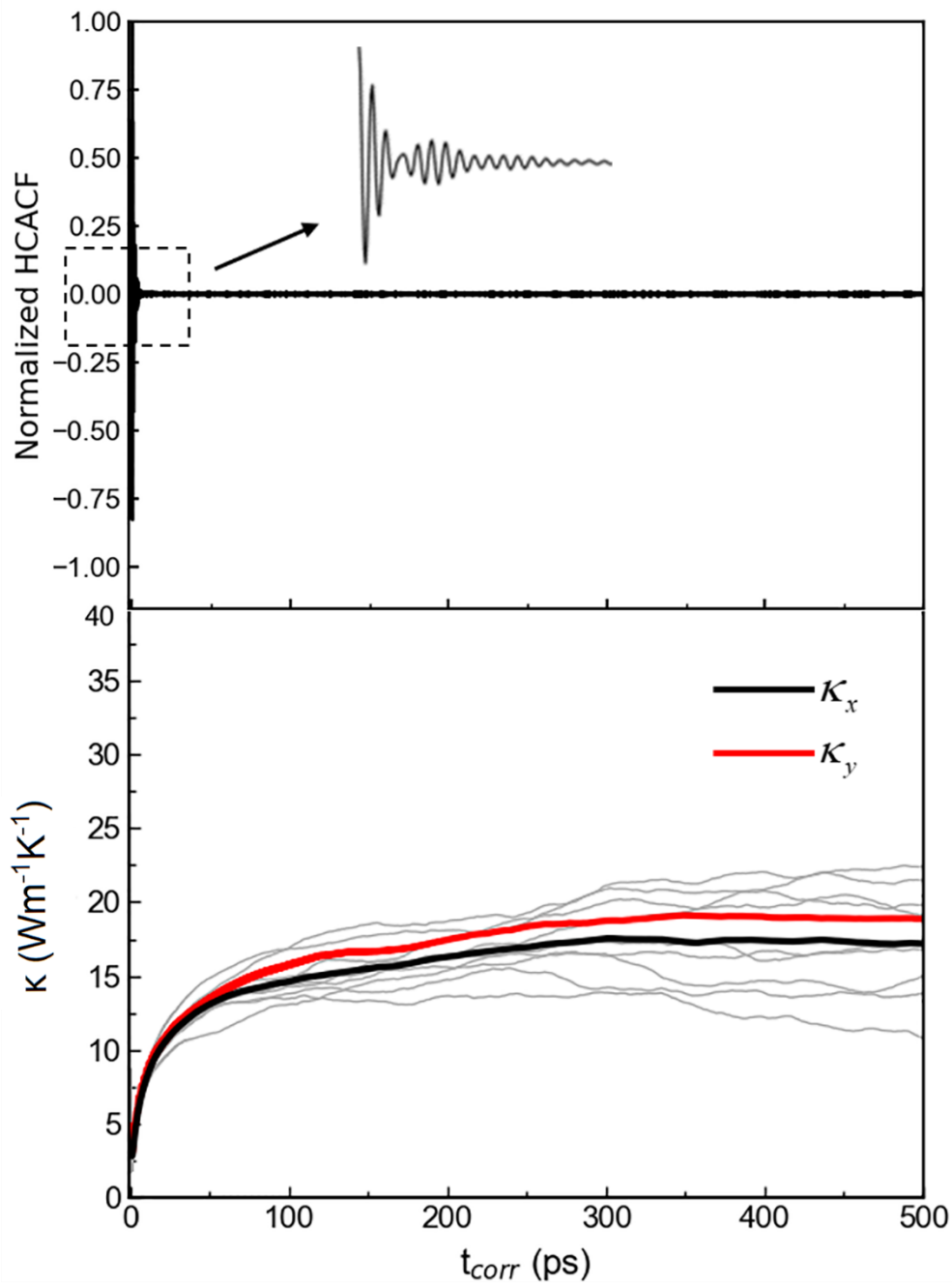

Figure 4. Normalized heat current auto-correlation function (HCACF) of a single MD run for the unstrained HBPN. Running integrals used to estimate the thermal conductivity obtained by averaging over 10 independent simulations. The light-gray curves represent the thermal conductivities for each of the 10 independent simulations and the super imposed thick curves represent the corresponding average values. For simplicity, only the 10 independent runs for κ_x are shown by light grey solid lines.

According to the findings of Mashhadzadeh *et al.*[7], uniaxial tension could lead to the rising of κ inside BPN in both zigzag and armchair directions. By increasing the strain from 1% to 5%, the κ increased from 111.3 to 147.2 $Wm^{-1}K^{-1}$. Yang *et al.*[48] also demonstrated that the strain generated by biaxial stretching also increases the κ of the original BPN. At a biaxial tensile strain of 5%, the room temperature κ of BPN is approximately 4-5 times that of the original configuration. Therefore, it can be seen that both uniaxial and biaxial strains can cause an increase in the κ of BPN. To study the strain effect on the thermal transport properties of HBPN, uniaxial strain is applied to the structure. Previous results from Hu[51], Cui[38] and Zhang[50] *et al.* focused only on the evolution of κ of the structure in the stretching direction. Here we analyzed thermal conductivities in both directions under uniaxial tension. The κ values and anisotropy ratios under various strains after uniaxial stretching in each direction were calculated and depicted in Fig. 5. Firstly, values of κ_x and κ_y hardly change obviously until the strain rate reached ε = 15% independent the direction in which the strain was loaded. Then the κ increases until the final structure's fracture. When the strain was loaded in the zigzag direction until ε = 25%, values of κ_x and κ_y increased to $\kappa_x \pm \Delta\kappa_x = 69.424 \pm 9.027$ $Wm^{-1}K^{-1}$ and $\kappa_y \pm \Delta\kappa_y = 24.129 \pm 1.957$ $Wm^{-1}K^{-1}$ (a factor of 4.022 and 1.256 times in *x* and *y* directions, respectively). The thermal anisotropy ratio $p(zz)$ increased from 0.898 to 2.877. For comparison, when the strain was loaded in the armchair direction until ε = 30%, values of κ_x and κ_y increased to $\kappa_x \pm \Delta\kappa_x = 27.507 \pm 4.593$ $Wm^{-1}K^{-1}$ and $\kappa_y \pm \Delta\kappa_y = 67.1024 \pm 7.276$ $Wm^{-1}K^{-1}$ (increased by a factor 1.637 and 3.422 times in *x* and *y* directions, respectively). The thermal anisotropy ratio $p(ac)$ also increased from 1.167 to 2.439 indicating that κ is more sensitive when stretching along the zigzag direction. From the figure, we observed that values of κ_x and κ_y both increased under uniaxial strain larger than ε = 15%. However, the increase rate of κ in the perpendicular direction is relatively smaller than that in the stretched direction. Therefore, the anisotropy ratio always increased gradually from its definition. Similar to BPN, the κ of HBPN under strain is generally in an upward trend. Increased strain resulted in increased bond length and weaker atomic interactions, resulting in a drop in phonon rate scattering and a rise in κ[51].

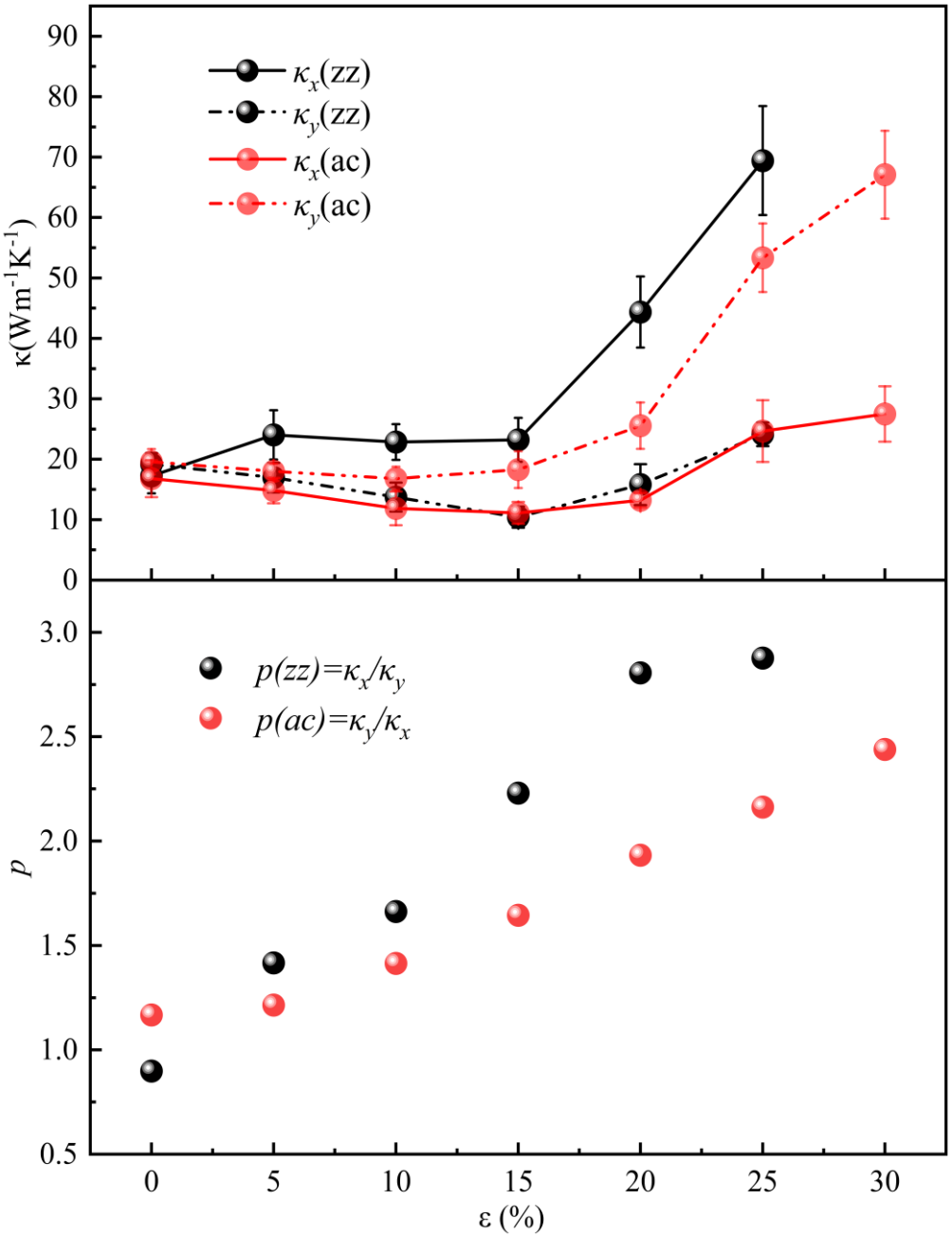

Figure 5. Variation of the EMD-predicted thermal conductivity of HBPN κ at 300 K in uniaxial stretching along the zigzag (black lines) and armchair (red lines) directions (upper panel). Each bar shows the results of 10 independent simulations with standard error overlaid on the top. Correspondingly, anisotropy ratios ($p(zz)=\frac{\kappa_x}{\kappa_y}$ and $p(ac)=\frac{\kappa_y}{\kappa_x}$) for different strains in each direction are also given in the lower panel.

The strain caused modifications of the atomic distances, interactions between atoms and even the crystal geometry and thus the effective volume of the model. In EMD method of calculating thermal conductivity, the volume of the structure is a required term in the Green-Kubo formula (*eq.* 1.1) to get κ. We have taken into account this variation. To obtain the volume variation of the structure under strain the thickness of the quasi-two dimensional HPBN under different strains are given in Fig. 6. Similar to the previously studied silicene, polyethylene[52] and some defective graphene structures[53,54], HBPN is also a buckling material. During the stretching process, the buckling HBPN will become more and more flattened by adjusting the two different C atomic layer distances. When $\varepsilon < 15\%$, the thickness of the HBPN model *d* declined slowly with uniaxial strain and then it decreased quickly after $\varepsilon > 15\%$ which was why the κ increased quickly within this range.

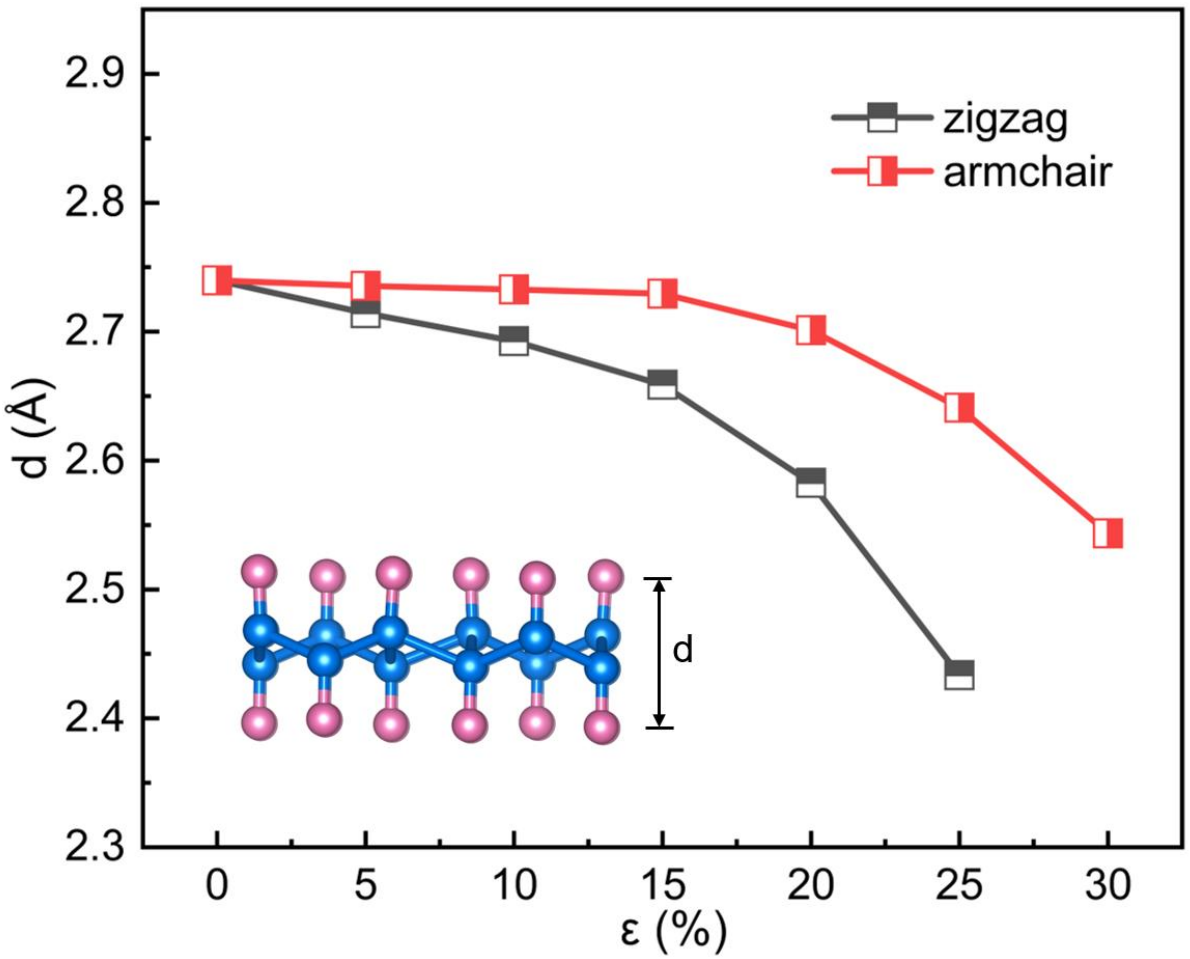

Figure 6. The thickness of the HBPN model *d* change with uniaxial strain along the zigzag (black line with half-solid symbols) and armchair (red line with half-solid symbols) directions before the break of structure occurred.

Compared to the thermal transport properties of other 2D materials like graphene[55], 1D graphene nanoribbon and carbon nanotube[56], the behavior of HBPN's κ under uniaxial tension was very different although they are all graphene derivatives made of the same C atoms. Previous results showed that thermal conductivities of graphene and graphene nanoribbons descended under tension[57] while those values of HBPN would increase under similar structure's deformation like buckling silicene[58]

and polyethylene (PE) chain[59]. However, HBPN can withstand a much greater strain extent, lower fracture κ and lower increasing rate of κ under tension. Take κ_x (κ_y) under tension to analyze, when the tensile strain reaches 25% (30%) in zigzag (armchair) direction, the κ_x (κ_y) increases by about ~ 4 (3.4) times. For buckling silicene, its κ increased by about 6.7 times when stretched to 4 %, reaching ~ 242.5 $Wm^{-1}K^{-1}$[60]. While for the PE chain, its κ would increase by 7.2 times under 30 % tension, reaching 181.28 $Wm^{-1}K^{-1}$ [61]. Therefore, HBPN is more suitable than the aforementioned materials as thermoelectric conversion material under a larger stretch condition.

To elucidate the intrinsic physical mechanism of the effect of strain on the heat transfer of HBPN, we calculated the PDOS of HBPN and its *x*, *y* and *z* components under uniaxial strain, as plotted in Fig. 7. Larger PDOS values regions were found at lower disperse (~ 10-60 THz) and higher narrow (~ 80-90 THz) frequency ranges (Fig. 7 (a) and (e)) which were zoomed in to deeply understand the behavior of phonons under strain.

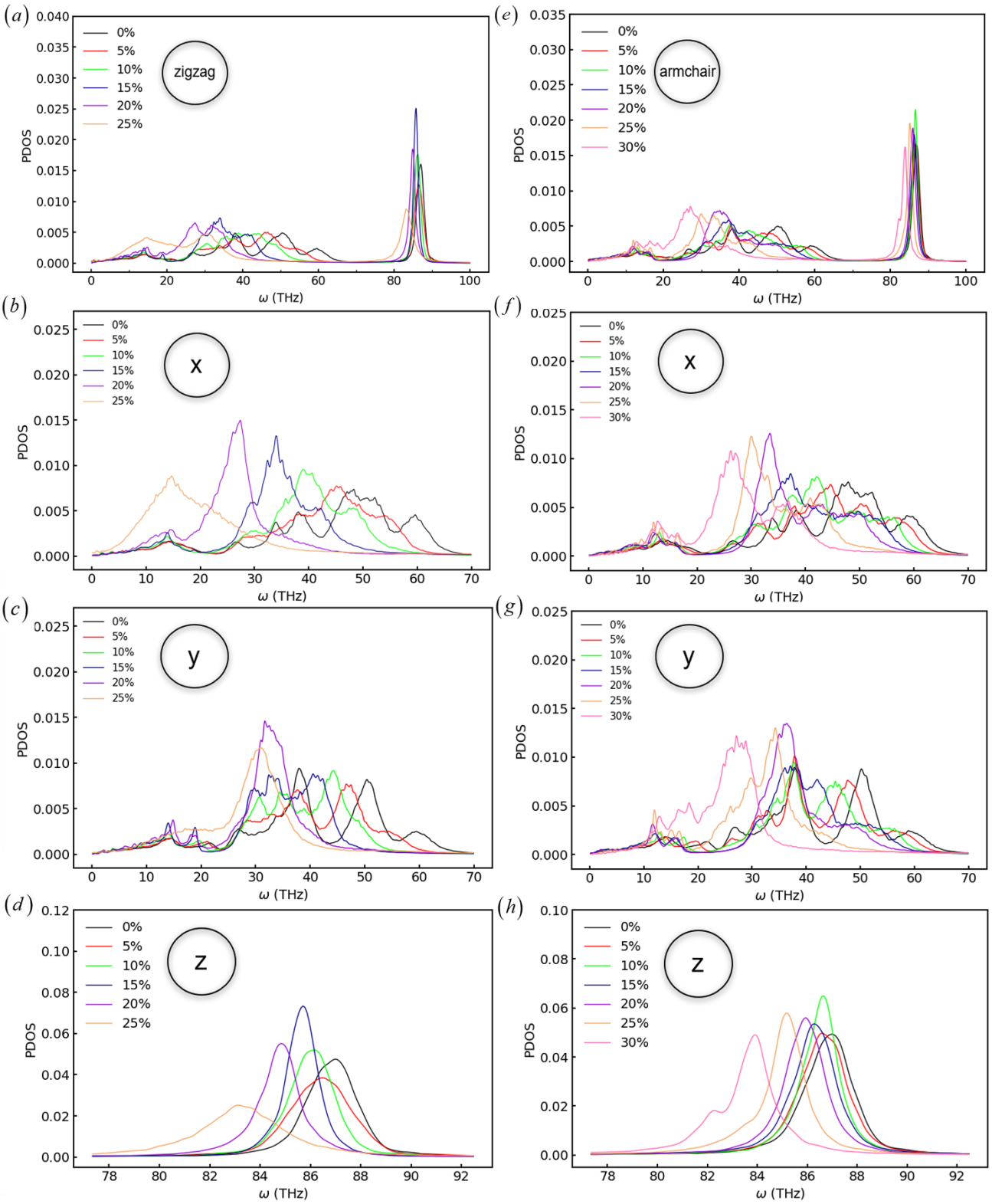

Figure 7. Total PDOS ((a) and (e)) and its partial components in *x*, *y* and *z* directions of HBPN under strain along (a-d) zigzag and (e-h) armchair directions, respectively.

On the one hand, let's look at the lower-frequency phonons with in-plane phonon modes (*i.e. x* and *y* components). From the figure, it's observed that the phonons shifted to left with height and width of the main PDOS wave increased with strain, indicating that the number of lower-frequency phonons went up. From the classical lattice heat transfer theory, higher peaks carried more energy with weaker phonon scattering and thus improved the heat transfer performance of the material. On the other hand, wave packet peak position of higher-frequency phonons with out-of-plane curvature phonon modes (*i.e. z* component) also moved to left a little with amplitude decreased obviously after $\varepsilon > 15\%$, indicating that the number of higher-frequency phonons degraded. Huo *et al.* proposed that the scattering mechanism of surface low-coordination atoms to phonons, indicating that the scattering rate was proportional to the 4^{th} power of phonon frequency[62]. Besides, higher-frequency phonons located in a narrow frequency region demonstrating that the lowered number of phonons and thus the caused lowered scattering rate played an important role in raising thermal conductivity.

Additionally, with the increase of tensile strain, the bond length between atoms increased and the buckling distance decreased. The fact that the structure became flatter and flatter could help significantly reduce the coupling between flexural acoustic modes (*i.e. z* direction vibration phonons) and in-plane phonon modes (*i.e. x* and *y* direction vibration phonons), which significantly weakened the scattering between these modes[60]. Using the similar analysis method, the thermal conductivity of silicene[63] and PE chain[61,64] were found to increase with strain.

C. Wave-packet propagation analysis

The WP Propagation simulations are depicted in the Figs. 8 and 9 where we present the results obtained for wave-packets along the armchair and zigzag direction, respectively. Each column

corresponds to a specific strain state (unstrained, strain along armchair and along zigzag direction) and each row to a specific polarization of the excited phonon. Each element of specific strain state and polarization consists of a series of snapshots of the kinetic energy per atom map on the left, taken every 25 fs (starting from $t = 25$ ps).

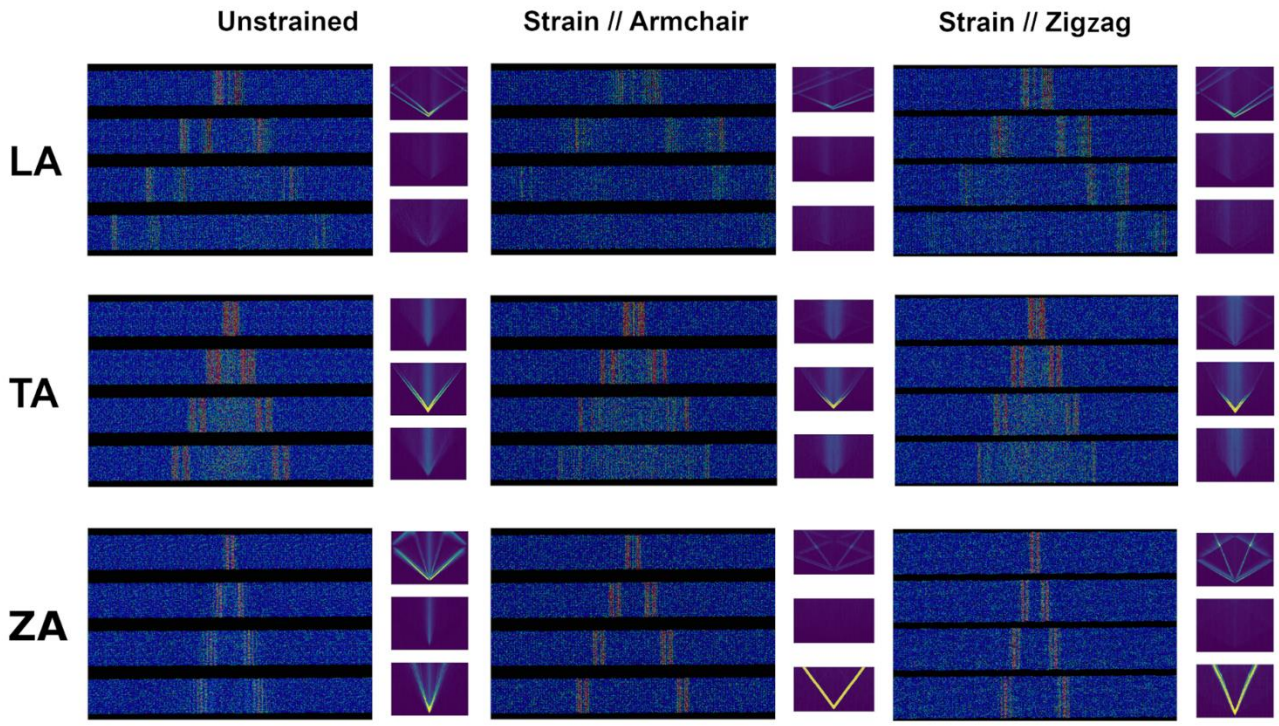

Figure 8. Armchair direction of propagation: Snapshots of kinetic energy maps every 25 fs and polarization-resolved kinetic energy profiles for all polarizations (LA, TA, ZA) and strain states (unstrained, strained along the armchair direction, strain along the zigzag direction). For the KE profiles, the color map limits are 16-155 meV/atom, the horizontal (length) axis limits correspond to the entire lengths of the studied structures, while the vertical (time) axes correspond to the entire simulation times (0-5 ps). Note that for the LA components, there is an apparent reflection at the edges of the structure, due to the periodic boundary conditions (similarly hereinafter).

On the right we present the polarization-resolved kinetic energy profiles, with the top, middle and

bottom figures corresponding to kinetic energy due only to the longitudinal, transverse and flexural components of the velocities, respectively, given by

$$E_a = \frac{1}{2} m v_a^{\,2} \tag{1.5}$$

where a corresponds to the projection of the velocity along a particular direction. In our calculations the zigzag axis of HBPN was placed along the x-axis. Therefore, for a WP travelling along the armchair direction, the LA component of the kinetic energy corresponds to E_y, the TA to E_x, etc.

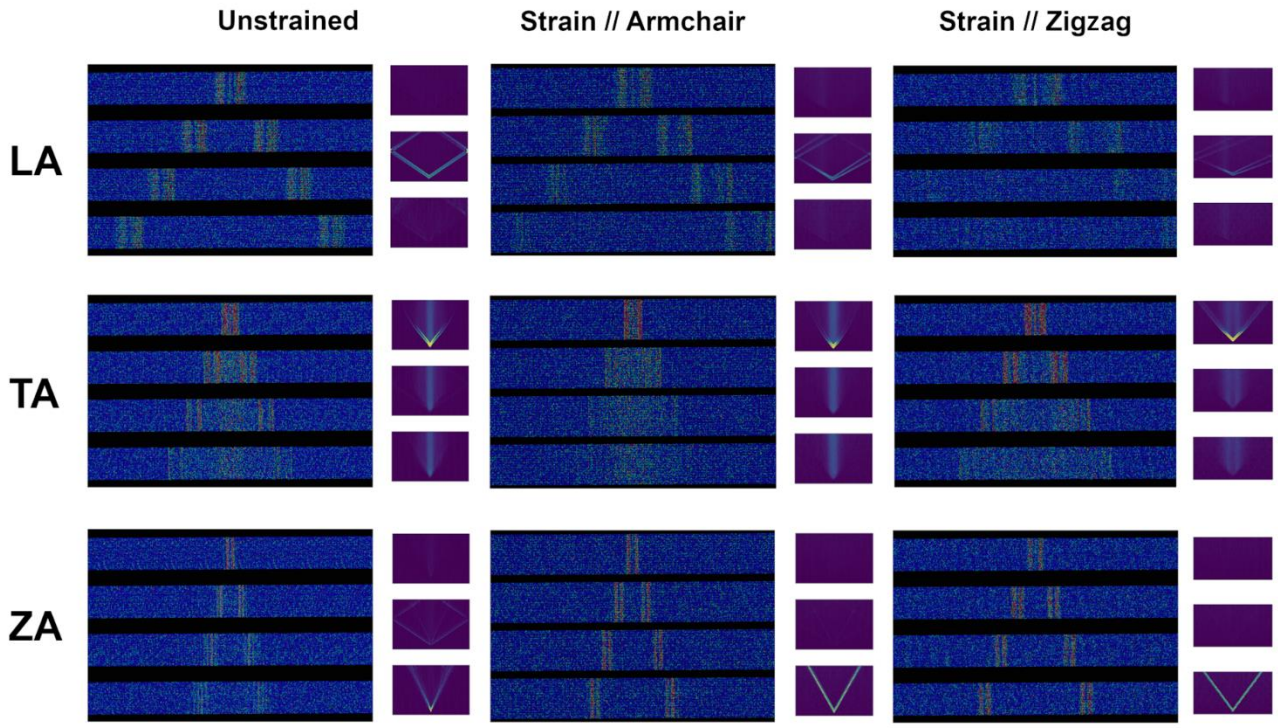

Figure 9. Zigzag direction of propagation: Snapshots of kinetic energy maps every 25 fs and polarization-resolved kinetic energy profiles for all (LA, TA, ZA) and strain states (unstrained, strained along the armchair direction, strain along the zigzag direction). For the KE profiles, the color map limits are 16-155 meV/atom, the horizontal (length) axis limits correspond to the entire lengths of the studied structures, while the vertical (time) axes correspond to the entire simulation times (0-5 ps).

By following the time evolution of the wave packets, the group velocities of the excited phonons were also calculated. The results for the phonons with wave vectors parallel to the armchair and zigzag direction are presented in Tab. 1 and Tab. 2, respectively.

Table 1: Armchair direction: Phonon group velocities for all polarizations and all strain states

× (10^3 m/s)	No Strain	Strain // Armchair	Strain // Zigzag
v_g^{LA}	15.1	26.3	15.9
v_g^{TA}	7.2	8.4	7.5
v_g^{ZA}	5.4	7.3	5.6

Table 2: Zigzag direction: Phonon group velocities for all polarizations and all strain states

× (10^3 m/s)	No Strain	Strain // Armchair	Strain // Zigzag
v_g^{LA}	14.9	18.1	26.3
v_g^{TA}	7.4	7.4	8.8
v_g^{ZA}	5.3	5.5	7.6

By comparing the values obtained, one can directly make the following observations: First of all, the armchair and zigzag directions (in the unstrained configuration) have practically the same group velocities, while the application of strain along the axis of propagation increases the velocities of all polarizations, compared to the unstrained case. The LA group velocity is the most affected, with a 75% increase. Additionally, strain applied in the perpendicular direction doesn't affect the velocities, with

the exception of the LA mode along the zigzag direction, which is also increased, but less compared to the configuration strained parallel to the propagation axis.

Furthermore, as can be seen in Fig.10, excitation of a ZA phonon simultaneously results in a creation of an LA phonon as well, indicating a strong coupling between the two acoustic modes. This can be easily understood by considering the fact that in order to create an out-of-plane ripple in a quasi-2D ribbon with fixed ends, the material has to be stretched along its length to accommodate for the ripples, thus creating a longitudinal wave.

The ZA acoustic phonons also exhibit dispersion. The wave packet components have slightly different group velocities and as a result, the total WP spreads as it propagates (see Fig.10, right). This is a consequence of the fact that in HBPN the ZA acoustic branches are parabolic and thus the group velocities of ZA phonons with different k-vectors are not constant. This is in fact a known behaviour common in 2D materials and it is a result of their plane symmetry[65].

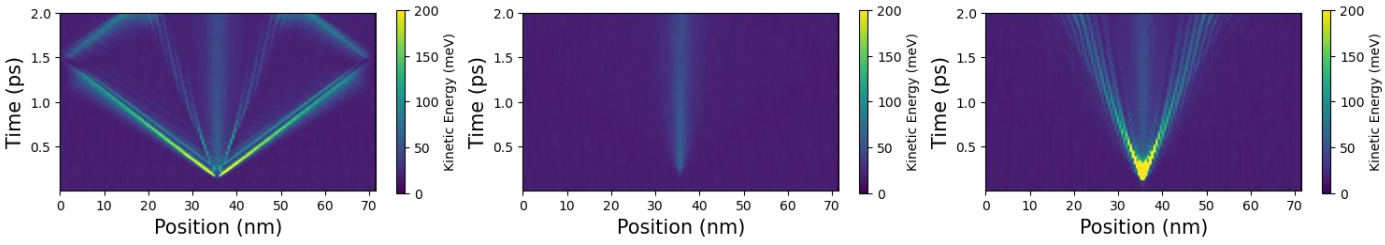

Figure 10. Kinetic energy profiles for a ZA phonon wave-packet along the armchair direction in an unstrained HBPN ribbon. The figures show the polarization-resolved profile, for the LA (left), the TA (middle) and the ZA components (left). The colormap limits are 0 (purple) to 200 meV/atom (yellow).

One shall also notice that in the length and time scales that we have investigated in this study, the phonon wave-packets that we excited do not all exhibit exponential decay, with the notable exception of the transverse modes, which decay exponentially in even shorter time scales and quickly thermalize

with the phonon heat bath background. This can be seen more clearly in Fig.11, where we present the kinetic energy map evolution (left), the polarization-resolved kinetic energy profile (middle) and the tracking of the position and height of the center of the kinetic energy wave packet.

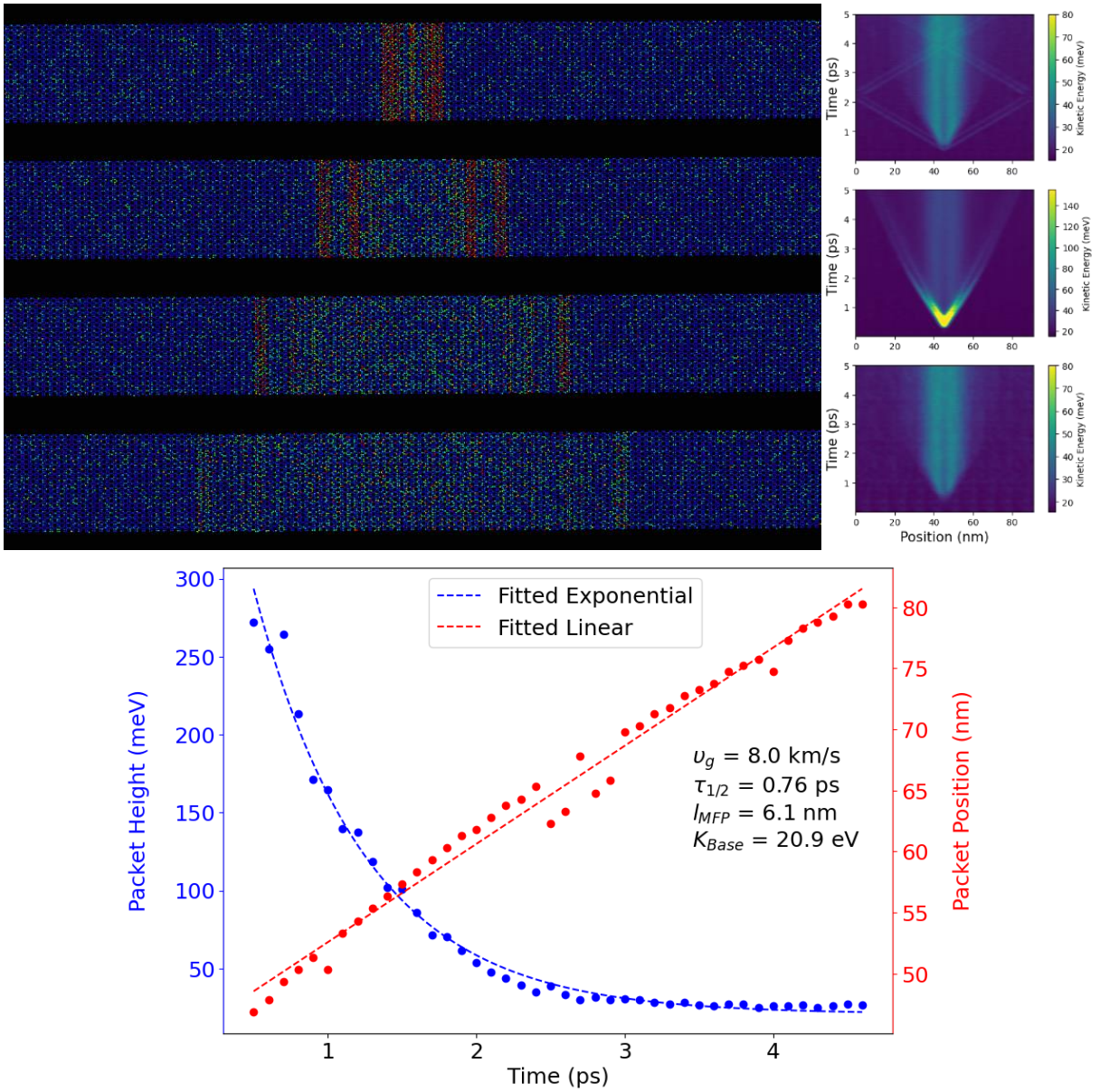

Figure 11. Exponential decay of a TA phonon wave packet along the armchair direction in an HBPN ribbon strained along the same direction. Top Left: Time evolution of the kinetic energy map. Top Right: Kinetic energy profile resolved for all three polarizations along the armchair direction. The colormap limits are from 16 (purple) to 80 meV/atom (yellow) for the LA and ZA components, while for the TA the upper limit

(yellow) becomes 155 meV/atom for better contrast. Bottom: Time evolution of the position and the height of the wave packet centre. The results of fitting to obtain their lifetimes and mean free paths are also visible.

In order to obtain quantitative results, we trace the position and height of the center of the wave packet with respect to time. By fitting them with a linear and exponential fit respectively, we can obtain the group velocity v_g and the exponential decay rate $\tau_{1/2}$.The heat profile shows a diffuse transfer of kinetic energy from the excited TA mode to all other modes equally, which is an indication of diffuse anharmonic scattering. The positions show a clear linear trend implying a constant group velocity, which was found to be $v_g = 8 \cdot 10^3 m/s.$ The energy wave packet's height also shows a strong exponential decay. After fitting, we obtain the exponential decay constant of $\tau_{1/2}$=$0.76 ps$, which we attribute to the phonon's lifetime. The corresponding phonon Mean Free Path (MFP), which is calculated by

$$l_{MFP} = v_g \cdot \tau_{1/2} \tag{1.6}$$

was found to be $l_{MFP} = 6.1 nm.$

For the other polarizations, the length and time scales needed to capture their decay were much larger and the computational effort for their calculation was exceeding the interests of this work. However, for illustration purposes, we performed a much longer simulation for a much larger structure, in order to calculate the lifetime and MFP of the LA phonon along the zigzag direction, for an unstrained HBPN ribbon. The results shown in Fig. 12 clearly indicate that this phonon decays exponentially with a lifetime of $\tau_{1/2}$=$7.47 ps$ and a MFP of $l_{MFP} = 114.3 nm$, which is much larger than the length scales used in the main calculations.

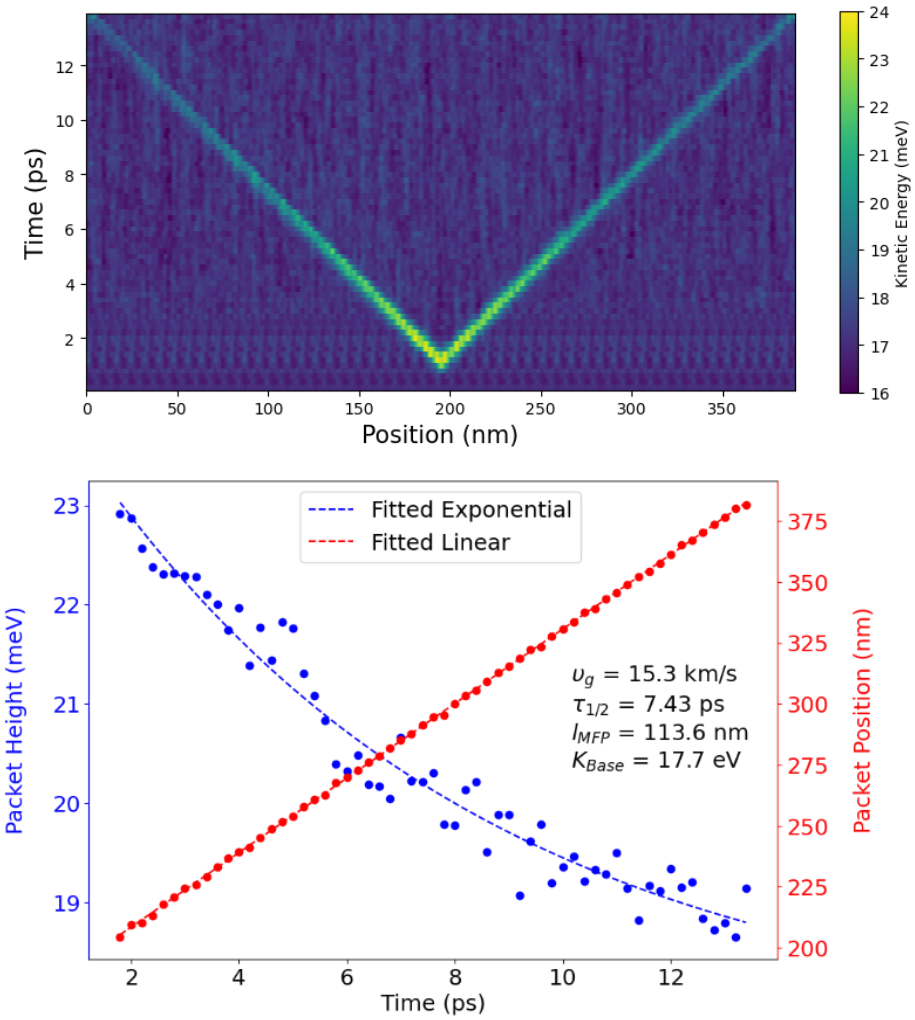

Figure 12. Kinetic energy profile (top) and tracing of the wave-packet peak (bottom) for an LA phonon wave-packet along the zigzag direction in an unstrained HBPN ribbon. By fitting the position and the height of the wave-packet centre with respect to time, we obtain the group velocity v_g and the exponential decay rate $\tau_{1/2}$.The KE map colormap limits are from 16 (purple) to 24 meV/atom (yellow).

IV. Summary and conclusions

In summary, mechanical and thermal transport properties of hydrogenated biphenylene network was studied systematically by molecular dynamics simulations. The absence of imaginary phonon frequencies indicated that the fully hydrogenated biphenylene network structure was mechanically

stable. Mechanical properties investigation indicated that HBPN could sustain a strain as large as $\varepsilon =$ 28.8% and 34.5% along the zigzag and armchair directions, respectively, with the corresponding Young's modulus of 326.32 and 264.94 GPa. Besides, the thermal conductivity of HBPN exhibited an anomalous response to uniaxial tensile strain. Different from its mother 2D material like graphene, the κ of HBPN first fluctuated at a plateau with applied tensile strain and then increased significantly rapidly. By correlating the velocity autocorrelation function, the phononic density of states was obtained to explain the relative contribution of phonons to the κ in each phonon mode. The increase of PDOS peak at low frequency region indicated that more excited phonons carried more energy could help improve thermal conductivity. Besides, the reduction of the number of higher-frequency phonons caused weakening of the phonon-surface scattering was another factor to increase thermal conductivity. Finally, the strain induced flattening of the structure could help weaken the coupling between phonons with in-plane and curvature vibrational modes.

WP Propagation method within MD was employed to analyze the propagation of phonons inside the HBPN and group velocities, phonon lifetimes and mean free paths were obtained. First of all, the armchair and zigzag directions (in the unstrained configuration) have practically the same group velocities. Besides, the calculations show that strain generally increases the phonon group velocities, but it practically affects them only when it is applied along the axis of propagation, and the longitudinal (LA) modes are the most affected with as much as 75% increase. A strong coupling between the LA and ZA modes is observed, while the ZA phonon wave-packets exhibit dispersion due to their-non-linear dispersion curves. Finally, while the LA and ZA modes have Mean Free Paths exceeding 100 nm, the TA modes decay particularly fast, with a MFP around 6 nm, due to their small lifetimes, which

are found to be <1 nm.

The results obtained would be beneficial to understand how to modulate the thermal transport properties of 2D structures with strain engineering, as would be use potential in tuning their electronic and thermoelectric properties for applications.

CRediT

Yang Han developed the idea. Xiaowei Zhang and Markos Poulos performed all numerical calculations, analyzed results and wrote the manuscript. Konstantinos Termentzidis and Yang Han analyzed results and revised the manuscript. Donglei Zhao, Tengfei Zhang, Xiaochuang Liu participated in data processing. Shijie Jia and Guolei Zhang participated in article revision. All the authors read and approved the final manuscript.

Conflicts of interest

There are no conflicts of interest to declare.

Supporting Information

12 hydrogenated biphenylene networks configuration design and its corresponding energies.

Acknowledgements

The authors acknowledge the financial support from the National Natural Science Foundation of China with No. 12104111. We are grateful for computational resources support from the High-

Performance Computing Center of Collaborative Innovation Center of Advanced Microstructures and Beijing Super Cloud Computing Center. Xiaowei Zhang gratefully acknowledges fruitful discussions with Junyu Hu, Hangbing Liu, Minghui Chen, Hao Bai and Yue Liang.

References

1. Chen X K, Zeng Y J, Chen K Q. Thermal Transport in Two-dimensional Heterostructures. *Front. Mater.* **2020**, *7*, 578791.
2. Ghany N A A, Elsherif S A, Handal H T. Revolution of Graphene for Different Applications: State-of-the-art. *Surf. Interfaces* **2017**, *9*, 93-106.
3. Novoselov K S, Geim A K, Morozov S V, Jiang D, Zhang Y, Dubonos S V, Grigorieva I V, Firsov A A. Electric Field Effect in Atomically Thin Carbon Films. *Science* **2004**, *306*, 666-669.
4. Fan Q, Yan L, Tripp M W, Krejčí O, Dimosthenous S, Kachel S R, Chen M, Foster A S, Koert U, Liljeroth P, et al. Biphenylene Network: A Nonbenzenoid Carbon Allotrope. *Science* **2021**, *372*, 852-856.
5. Ke K, Meng K, Rong J, Yu X. Biphenylene: A Two−dimensional Graphene−based Coating with Superior Anti−corrosion Performance. *Materials* **2022**, *15*, 5675.
6. Li Q, Zhou J, Liu G, Wan X G. Extraordinary Negative Thermal Expansion of Monolayer Biphenylene. *Carbon* **2022**, *187*, 349-353.
7. Hamed Mashhadzadeh A, Zarghami Dehaghani M, Molaie F, Fooladapanjeh S, Farzadian O, Spitas C. A Theoretical Insight into the Mechanical Properties and Phonon Thermal Conductivity of Biphenylene Network Structure. *Comp. Mater. Sci.* **2022**, *214*, 111761.
8. Ying P, Liang T, Du Y, Zhang J, Zeng X, Zhong Z. Thermal Transport in Planar Sp2-hybridized Carbon Allotropes: A Comparative Study of Biphenylene Network, Pentaheptite and Graphene. *Int. J. Heat Mass Tran.* **2022**, *183*, 122060.
9. Wang K, Ren K, Zhang D, Cheng Y, Zhang G. Phonon Properties of Biphenylene Monolayer by First-principles Calculations. *Appl. Phys. Lett.* **2022**, *121*, 042203.
10. Liu T, Jing Y, Li Y. Two-Dimensional Biphenylene: A Graphene Allotrope with Superior Activity toward Electrochemical Oxygen Reduction Reaction. *J. Phys. Chem. Lett.* **2021**, *12*, 12230-12234.
11. Bianco V, De Rosa M, Vafai K. Phase-change Materials for Thermal Management of Electronic Devices. *Appl. Therm. Eng.* **2022**, *214*, 118839.
12. He Z, Yan Y, Zhang Z. Thermal Management and Temperature Uniformity Enhancement of Electronic Devices by Micro Heat Sinks: A Review. *Energy* **2021**, *216*, 119223.
13. Mo S, Seo J, Son S K, Kim S, Rhim J W, Lee H. Engineering Two-dimensional Nodal Semimetals in Functionalized Biphenylene by Fluorine Adatoms. *arXiv 2401.17607.*
14. Son Y W, Jin H, Kim S. Magnetic Ordering, Anomalous Lifshitz Transition, and Topological Grain Boundaries in Two-dimensional Biphenylene Network. *Nano Lett.* **2022**, *22*, 3112-3117.
15. Hou Y, Ren K, Wei Y, Yang D, Cui Z, Wang K. Opening a Band Gap in Biphenylene Monolayer

via Strain: A First-Principles Study. *Molecules* **2023**, *28*, 4178.
16. Ren X, Wang K, Yu Y, Zhang D, Zhang G, Cheng Y. Tuning the Mechanical Anisotropy of Biphenylene by Boron and Nitrogen Doping. *Comp. Mater. Sci.* **2023**, *222*, 112119.
17. Xie Y, Chen L, Xu J, Liu W. Effective Regulation of the Electronic Properties of a Biphenylene Network by Hydrogenation and Halogenation. *RSC Adv.* **2022**, *12*, 20088-20095.
18. González-Herrero H, Gómez-Rodríguez J M, Mallet P, Moaied M, Palacios J J, Salgado C, Ugeda M M, Veuillen J Y, Yndurain F, Brihuega I. Atomic-scale Control of Graphene Magnetism by Using Hydrogen Atoms. *Science* **2016**, *352*, 437-441.
19. Slot M R, Gardenier T S, Jacobse P H, Van Miert G C P, Kempkes S N, Zevenhuizen S J M, Smith C M, Vanmaekelbergh D, Swart I. Experimental Realization and Characterization of an Electronic Lieb Lattice. *Nature Phys* **2017**, *13*, 672-676.
20. Møller M, Jarvis S P, Guérinet L, Sharp P, Woolley R, Rahe P, Moriarty P. Automated Extraction of Single H Atoms with STM: Tip State Dependency. *Nanotechnology* **2017**, *28*, 075302.
21. Shen H, Yang R, Xie K, Yu Z, Zheng Y, Zhang R, Chen L, Wu B R, Su W S, Wang S. Electronic and Optical Properties of Hydrogen-terminated Biphenylene Nanoribbons: A First-principles Study. *Phys. Chem. Chem. Phys.* **2022**, *24*, 357-365.
22. Stuart S J, Tutein A B, Harrison J A. A Reactive Potential for Hydrocarbons with Intermolecular Interactions. *J. Chem. Phys.* **2000**, *112*, 6472-6486.
23. Sharifi M, Heidaryan E. Thermal Rectification in Ultra-narrow Hydrogen Functionalized Graphene: A Non-equilibrium Molecular Dynamics Study. *J Mol Model* **2022**, *28*, 298.
24. Lee S, Singh A, Lee H. Band Gap Engineering of 2D Biphenylene Carbon Sheets with Hydrogenation. *J. Korean Phys. Soc.* **2021**, *79*, 846-850.
25. Han Y, Dong J, Qin G, Hu M. Phonon Transport in the Ground State of Two-dimensional Silicon and Germanium. *RSC Adv.* **2016**, *6*, 69956-69965.
26. Thomas J A, Iutzi R M, McGaughey A J H. Thermal Conductivity and Phonon Transport in Empty and Water-filled Carbon Nanotubes. *Phys. Rev. B* **2010**, *81*, 045413.
27. Kresse G, Furthmüller J. Efficient Iterative Schemes for *ab initio* Total-energy Calculations Using a Plane-wave Basis Set. *Phys. Rev. B* **1996**, *54*, 11169-11186.
28. Perdew J P, Burke K, Ernzerhof M. Generalized Gradient Approximation Made Simple. *Phys. Rev. Lett.* **1996**, *77*, 3865-3868.
29. Perdew J P. Density-functional Approximation for the Correlation Energy of the Inhomogeneous Electron Gas. *Phys. Rev. B* **1986**, *33*, 8822-8824.
30. Blöchl P E. Projector Augmented-wave Method. *Phys. Rev. B* **1994**, *50*, 17953-17979.
31. Chadi, D. J. Special Points for Brillouin-zone Integrations. *Phys. Rev. B* **1977**, *16*, 1746-1747.
32. Gonze X. First-principles Responses of Solids to Atomic Displacements and Homogeneous Electric Fields: Implementation of a Conjugate-gradient Algorithm. *Phys. Rev. B* **1997**, *55*, 10337-10354.
33. Togo A, Tanaka I. First Principles Phonon Calculations in Materials Science. *Scripta Mater.* **2015**, *108*, 1-5.
34. Khadem M H, Wemhoff A P. Comparison of Green–Kubo and NEMD Heat Flux Formulations for Thermal Conductivity Prediction Using the Tersoff Potential. *Comp. Mater. Sci.* **2013**, *69*,

428-434.
35. Alexander J S, Maxwell C, Pencer J, Saoudi M. Equilibrium Molecular Dynamics Calculations of Thermal Conductivity: A “How-to” for the Beginners. *CNL Nucl. Rev.* **2020**, *9*, 11-25.
36. Berendsen H J C, Postma J P M, Van Gunsteren W F, DiNola A, Haak J R. Molecular Dynamics with Coupling to an External Bath. *J. Chem. Phys.* **1984**, *81*, 3684-3690.
37. Morishita T. Fluctuation Formulas in Molecular-dynamics Simulations with the Weak Coupling Heat Bath. *J. Chem. Phys.* **2000**, *113*, 2976-2982.
38. Cui Q, Ren K, Zheng R, Zhang Q, Yu L, Li J. Tunable Thermal Properties of the Biphenylene and the Lateral Heterostructure Formed with Graphene: A Molecular Dynamics Investigation. *Front. Phys.* **2022**, *10*, 1085367.
39. Beltukov Y M, Fusco C, Parshin D A, Tanguy A. Boson Peak and Ioffe-regel Criterion in Amorphous Siliconlike Materials: The Effect of Bond Directionality. *Phys. Rev. E* **2016**, *93*, 023006.
40. Desmarchelier P, Carré A, Termentzidis K, Tanguy A. Ballistic Heat Transport in Nanocomposite: The Role of the Shape and Interconnection of Nanoinclusions. *Nanomaterials* **2021**, *11*, 1982.
41. Desmarchelier P, Tanguy A, Termentzidis K. Thermal Rectification in Asymmetric Two-phase Nanowires. *Phys. Rev. B* **2021**, *103*, 014202.
42. Desmarchelier P, Beardo A, Alvarez F X, Tanguy A, Termentzidis K. Atomistic Evidence of Hydrodynamic Heat Transfer in Nanowires. *Int. J. Heat Mass Tran.* **2022**, *194*, 123003.
43. Han Y, Yang J Y, Hu M. Unusual Strain Response of Thermal Transport in Dimerized Three-dimensional Graphene. *Nanoscale* **2018**, *10*, 5229-5238.
44. Han Y, Liang Y, Liu X, Jia S, Zhao C, Yang L, Ding J, Hong G, Termentzidis K. Stretched Three-dimensional White Graphene with a Tremendous Lattice Thermal Conductivity Increase Rate. *RSC Adv.* **2022**, *12*, 22581-22589.
45. Samadian M, Ajri M, Azizi A, Hemmatpour-Khotbesara M A. Investigating the Pinhole Effect on the Mechanical Properties of Biphenylene. *Appl. Phys. A* **2023**, *129*, 826.
46. Schelling P K, Phillpot S R, Keblinski P. Comparison of Atomic-level Simulation Methods for Computing Thermal Conductivity. *Phys. Rev. B* **2002**, *65*, 144306.
47. McGaughey A J H, Kaviany M. Phonon Transport in Molecular Dynamics Simulations: Formulation and Thermal Conductivity Prediction. *Advances in Heat Transfer*, **2006**, *39*, 169-255.
48. Yang G, Hu Y, Qiu Z, Li B L, Zhou P, Li D, Zhang G. Abnormal Strain-dependent Thermal Conductivity in Biphenylene Monolayer Using Machine Learning Interatomic Potential. *Appl. Phys. Lett.* **2023**, *122*, 082202.
49. Hu M, Zhang X, Poulikakos D. Anomalous Thermal Response of Silicene to Uniaxial Stretching. *Phys. Rev. B* **2013**, *87*, 195417.
50. Zhang Y Y, Pei Q X, He X Q, Mai Y W. A Molecular Dynamics Simulation Study on Thermal Conductivity of Functionalized Bilayer Graphene Sheet. *Chem. Phys. Lett.* **2015**, *622*, 104-108.
51. Einalipour Eshkalak K, Sadeghzadeh S, Molaei F. Interfacial Thermal Resistance Mechanism for the Polyaniline (C_3N)–Graphene Heterostructure. *J. Phys. Chem. C* **2020**, *124*, 14316-14326.
52. Shao C, Yu X, Yang N, Yue Y, Bao H. A Review of Thermal Transport in Low-dimensional

Materials Under External Perturbation: Effect of Strain, Substrate, and Clustering. *Nanosc. Microsc. Therm.* **2017**, *21*, 201-236.
53. Lherbier A, Roche S, Restrepo O A, Niquet Y M, Delcorte A, Charlier J C. Highly Defective Graphene: A Key Prototype of Two-dimensional Anderson Insulators. *Nano Res.* **2013**, *6*, 326-334.
54. Lherbier A, Dubois S M M, Declerck X, Roche S, Niquet Y M, Charlier J C. Two-dimensional Graphene with Structural Defects: Elastic Mean Free Path, Minimum Conductivity, and Anderson Transition. *Phys. Rev. Lett.* **2011**, *106*, 046803.
55. Li X, Maute K, Dunn M L, Yang R. Strain Effects on the Thermal Conductivity of Nanostructures. *Phys. Rev. B* **2010**, *81*, 245318.
56. Xu Z, Buehler M J. Strain Controlled Thermomutability of Single-walled Carbon Nanotubes. *Nanotechnology* **2009**, *20*, 185701.
57. Guo Z, Zhang D, Gong X G. Thermal Conductivity of Graphene Nanoribbons. *Appl. Phys. Lett.* **2009**, *95*, 163103.
58. Ding B, Li X, Zhou W, Zhang G, Gao H. Anomalous Strain Effect on the Thermal Conductivity of Low-buckled Two-dimensional Silicene. *NSR* **2021**, *8*, nwaa220.
59. He J, Kim K, Wang Y, Liu J. Strain Effects on the Anisotropic Thermal Transport in Crystalline Polyethylene. *Appl. Phys. Lett.* **2018**, *112*, 051907.
60. Xie H, Ouyang T, Germaneau É, Qin G, Hu M, Bao H. Large Tunability of Lattice Thermal Conductivity of Monolayer Silicene Via Mechanical Strain. *Phys. Rev. B* **2016**, *93*, 075404.
61. Zhang T, Luo T. Morphology-influenced Thermal Conductivity of Polyethylene Single Chains and Crystalline Fibers. *J. Appl. Phys.* **2012**, *112*, 094304.
62. Huo L, Xie G. Mechanism of Phonon Scattering by Under-coordinated Atoms on Surface. *Acta Phys.Sin.*, **2019**, *68*, 086501.
63. Kuang Y D, Lindsay L, Shi S Q, Zheng G P. Tensile Strains Give Rise to Strong Size Effects for Thermal Conductivities of Silicene, Germanene and Stanene. *Nanoscale,* **2016**, *8*, 3760-3767.
64. Shen S, Henry A, Tong J, Zheng R, Chen G. Polyethylene Nanofibres with Very High Thermal Conductivities. *Nat. Nanotechnol.* **2010**, *5*, 251-255.
65. Wirtz L, Rubio A. The Phonon Dispersion of Graphite Revisited. *Solid State Commun.* **2004**, *131*, 141-152.

TOC graphic

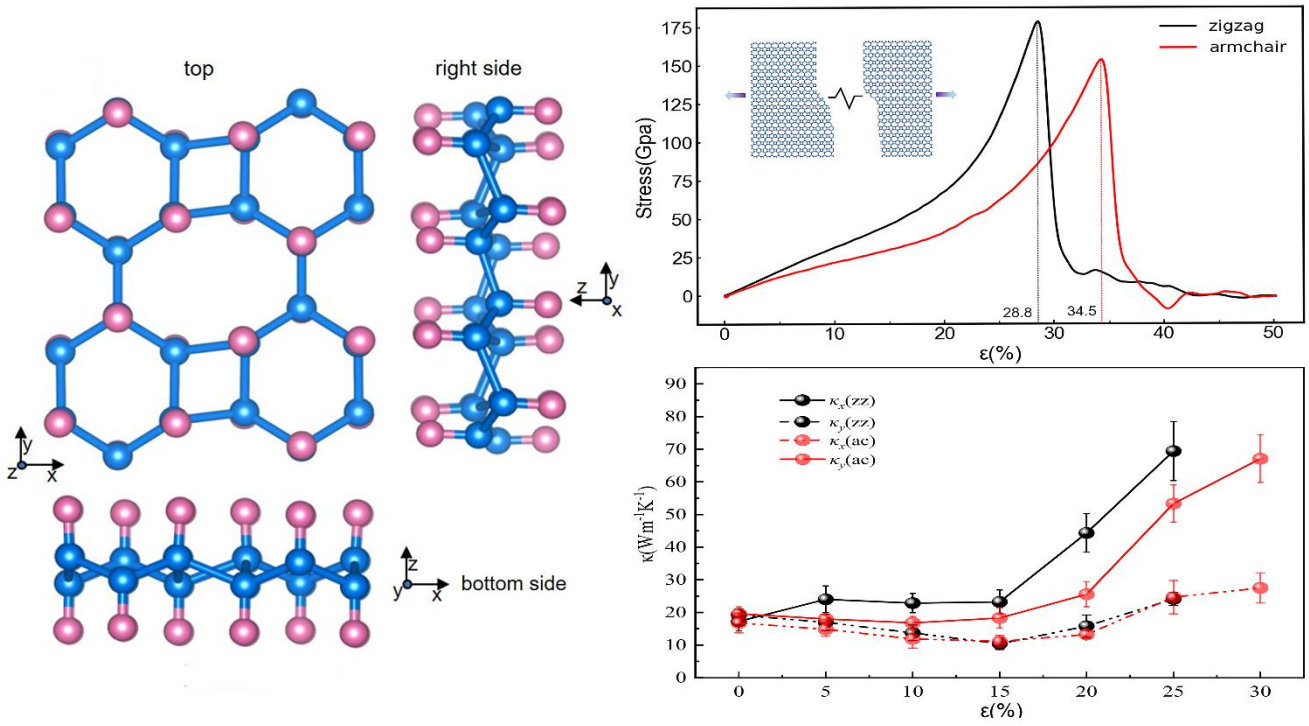
top
right side
bottom side
zigzag
armchair
Stress(Gpa)
ε(%)
28.8
34.5
κ_x(zz)
κ_y(zz)
κ_x(ac)
κ_y(ac)
κ(Wm^{-1}K^{-1})
ε(%)